Research Article

ADVANCED PHOTONICS

Transparent glassy composites incorporating lead-free anti-perovskite halide nanocrystals enable tunable emission and ultrastable X-ray imaging

Yakun Le,[a,†] Xiongjian Huang,[a,b,†] Hao Zhang,[a] Zhihao Zhou,[a] Dandan Yang,[a] Bozhao Yin,[a] Xiaofeng Liu,[c] Zhiguo Xia,[a] Jianrong Qiu,[d] Zhongmin Yang,[a,b] and Guoping Dong[a,*]

[a]South China University of Technology, School of Materials Science and Engineering, State Key Laboratory of Luminescent Materials and Devices, Guangzhou, China
[b]South China University of Technology, School of Physics and Optoelectronics, Guangzhou, China
[c]Zhejiang University, School of Materials Science and Engineering, Hangzhou, China
[d]Zhejiang University, College of Optical Science and Engineering, State Key Laboratory of Modern Optical Instrumentation, Hangzhou, China

Abstract. Lead halide perovskite materials exhibit excellent scintillation performance, which, however, suffer from serious stability and toxicity problems. In contrast, the heavy metal-free anti-perovskite materials $[MX_4]XA_3$ (A = alkali metal; M = transition metal; X = Cl, Br, I), a class of electron-inverted perovskite derivatives, exhibit robust structural and photophysical stability. Here, we design and prepare a lead-free $[MnBr_4]BrCs_3$ anti-perovskite nanocrystal (NC)-embedded glass for efficient X-ray-excited luminescence with high-resolution X-ray imaging with a spatial resolution of 19.1 lp mm^{-1}. Due to the unique crystal structure and the protection of the glass matrix, the Cs_3MnBr_5 NC-embedded glass exhibits excellent X-ray irradiation stability, thermal stability, and water resistance. These merits enable the demonstration of real-time and durable X-ray radiography based on the developed glassy composite. This work could stimulate the research and development of novel metal halide anti-perovskite materials and open a new path for future development in the field of high-resolution and ultrastable X-ray imaging.

Keywords: lead-free metal halides; anti-perovskite nanocrystals; glass; ultrastable X-ray imaging.

Received Apr. 11, 2023; revised manuscript received May 30, 2023; accepted for publication Jun. 12, 2023; published online Jul. 10, 2023.

[DOI: 10.1117/1.AP.5.4.046002]

1 Introduction

High-resolution and ultrastable X-ray imaging methods required in material inspection, medical diagnostics, astronomical discovery, and scientific research have stimulated extensive research on X-ray-responsive materials with high X-ray attenuation, efficient scintillation, fast light decay, and robust durability.[1–4] Recently, lead halide-based perovskites have attracted growing attention in the field of X-ray imaging, due to their excellent high luminescence efficiency, high X-ray attenuation ability, and short fluorescence lifetime.[5–8] However, they are restricted in the scintillation field due to the toxicity of heavy metal Pb, low photon yield caused by severe self-absorption effect, and poor X-ray irradiation stability.[9,10] In order to solve the above problems, many types of lead-free zero-dimensional (0D) metal halides,[11] such as Cu-based halides,[12–14] Ag-based halides,[15] Zr-based halides,[16] and Mn-based halides,[17,18] have been developed as effective scintillators for X-ray detection and imaging on account of their high photon yield, diversity of composition and structure, and unique self-trapped excitons luminescence mechanism. Nevertheless, most of them are fabricated in thin-film form or wafers for X-ray imaging,[11] which usually demonstrate low imaging resolution due to the light scattering by the large particles and crystal boundary.[9] In addition, lead-free 0D metal halides suffer from poor stability, especially in a hot and humid environment.[19] To improve the imaging resolution and durability, a more practical solution would be the encapsulation of the lead-free

*Address all correspondence to Guoping Dong, dgp@scut.edu.cn
†These authors contributed equally to this work.

0D metal halides with controllable size into a stable matrix. Recently, lead-free halide NCs have been crystalized in glass and exhibit potential in light-emitting devices,[20] but the dynamic X-ray imaging in a high-temperature and humid environment is hard to realize.

Compared with lead halide perovskite materials, the configuration of anti-perovskite materials can be represented as ABX_3, but electronically inverted (X is a cation, and A and B are anions or anionic groups).[21,22] From the point of view of structural chemistry, anti-perovskite can accommodate a variety of elements, forming a large family of functional materials. Anti-perovskite materials have shown various interesting properties, such as magnetism,[23] ionic conductivity,[24] superconductivity,[25] and negative thermal expansibility,[26] but have rarely been reported as photoluminescent materials. One type of anti-perovskite is $[MX_4]XA_3$ (A = alkali metal; M = transition metal; X = Cl, Br, I), in which the luminescence center is the $[MX_4]^{2-}$ tetrahedron filled in the three-dimensional (3D) XA_6 octahedral anti-perovskite skeleton. This unique structure can effectively reduce the interaction of the luminescence center and increase the spatial confinement effect so that anti-perovskite materials generally have high quantum efficiency and luminescence stability.[27] Recently, the specific requirements for performing X-ray imaging at high temperatures have increased dramatically. Nondestructive inspection of some high temperature industrial equipment can be done easily by X-ray imaging applications.[28,29] In addition, some investigation of the effects of high temperature on a polymer electrolyte fuel cell also needs high temperature X-ray imaging technology.[30,31] What is more, high-temperature X-ray microtomographic imaging can supply a new technique for studying mechanical behavior of multiphase composites.[32] Most importantly, the specific requirements for detectors used in space aimed at achieving stunning elevated temperature stability.[33,34] Therefore, it would be highly attractive to explore and design an anti-perovskite material for X-ray imaging applications in a high-temperature environment.

Here, we demonstrate state-of-the-art high-resolution and ultrastable X-ray imaging in a high-temperature and humid environment using the designed lead-free Cs_3MnBr_5 anti-perovskite nanocrystal (NC)-embedded glass. Mn^{2+} ions are transferred into Cs_3MnBr_5 NCs through *in situ* crystallization in the glass matrix during annealing, therefore displaying tunable luminescence color from red to green controlled by the annealing schedule. With the protection of the transparent glass matrix, Cs_3MnBr_5 NCs show excellent optical properties, good machinability, and high stability. As expected, the Cs_3MnBr_5 NC-embedded glass exhibits X-ray detection limit of 767 $nGy_{air}\,s^{-1}$, a high X-ray imaging spatial resolution of 19.1 $lp\,mm^{-1}$ and a high X-ray dose irradiation stability at 5.775 $mGy_{air}\,s^{-1}$. More importantly, this transparent NC–glass composite enables high-resolution X-ray imaging even in a high-temperature and humid environment. Our results would have strong implications for the development of next-generation X-ray imaging devices.

2 Results and Discussion

2.1 Synthesis and Structural Characterization of Cs_3MnBr_5 NCs in the Glass

A precursor glass (PG) containing cesium, manganese, and bromine elements is designed and fabricated by the melt-quenching method, and Cs_3MnBr_5 NCs are crystallized in the glass matrix by annealing above the glass transition (T_g) temperature (Fig. S1 in the Supplemental Material), as shown in Fig. 1(a). As a lead-free anti-perovskite material, the Cs_3MnBr_5 crystal consists of $[MnBr_4]^{2-}$ tetrahedrons filled in the (3D) $BrCs_6$ octahedral skeleton [Fig. 1(a)]. From the density functional theory (DFT) calculations of band structures and corresponding density of states [Figs. 1(b) and 1(c)], the direct bandgap of Cs_3MnBr_5 crystal is ~3.367 eV, contributing to the absorption band in the ultraviolet (UV) region and high optical transmittance in the visible region.[35] The diffraction peaks at 22.783 deg, 26.914 deg, and 29.454 deg corresponding to (004), (213), and (310) crystal facets of Cs_3MnBr_5 (PDF#27-0117) are observed in the X-ray diffraction (XRD) pattern after the glass was annealed at 570°C for 5 h [Fig. 1(d)]. In addition, X-ray photoelectron spectroscopy (XPS) was performed on the glass sample before and after annealing (Fig. S2 in the Supplemental Material). The characteristic peaks of Mn $2p_{1/2}$ (653.4 eV) and $2p_{3/2}$ (642.1 eV) are observed, which are higher than that in manganese halide (<640.7 eV), indicating that the electron density and covalent bond ratio of Cs_3MnBr_5 NC-embedded glass are increased.[36] This may result in stronger ionic bonding between manganese ions and bromine ions, which could enhance the stability under high-energy-ray irradiation.[17] The electron paramagnetic resonance (EPR) spectra show a wide EPR signal with a line width of 609.4 G instead of six fine structures because of the high concentration in the glass (Fig. S3 in the Supplemental Material).[37] The signal is more obvious after annealing, which is due to the stronger magnetic coupling caused by the decrease in the spacing of Mn^{2+} ions after the Cs_3MnBr_5 NCs crystallized in the glass.[38] A transmission electron microscope (TEM) image shows dispersed NCs with an average size of 18.3 nm, indicating the formation of NCs with good crystal quality in the glass matrix [Figs. 1(e) and 1(f)]. The crystal lattice fringes with a spacing of 0.305 nm can be seen in the high-resolution transmission electron microscope (HRTEM) image, which corresponds to the (310) crystal facet of Cs_3MnBr_5 [Fig. 1(g)]. The above results confirm the successful precipitation of Cs_3MnBr_5 NCs in the glass after annealing.

2.2 Photoluminescence Properties of Cs_3MnBr_5 NCs in the Glass

As a typical transition metal ion, the optical properties of Mn^{2+} ions are influenced by the strong interactions between electrons in their outermost d orbitals and their ligands, which can be described by the crystal field strength (10Dq) and the Racah parameter (B), respectively.[39,40] The Tanabe–Sugano diagram in Fig. 2(a) reveals the change in the energy level of Mn^{2+} as the electronic configuration of $3d_5$ is sensitive to local perturbations. The 10Dq and B for Mn (IV) in Cs_3MnBr_5 NCs are calculated to be 8192 and 811 cm^{-1}, and for Mn (VI) in glass are 11,306 and 732 cm^{-1}, respectively (see note 1 in the Supplemental Material). These calculations confirm that the $3d_5$ electronic configuration of Mn^{2+} doped in the glass was significantly changed after the crystallization of the glass.

The absorption spectra of the PG and the glass samples annealing at different temperatures are recorded in the wavelength region of 300 to 800 nm [Fig. 2(b)]. The narrow peak at 413 nm is attributed to the electronic transition of $^6A_1(S) \rightarrow {}^4A_1, {}^4E(G)$ of Mn^{2+} ions. Under the excitation of 365 nm UV light, a green emission band peaking at 523 nm

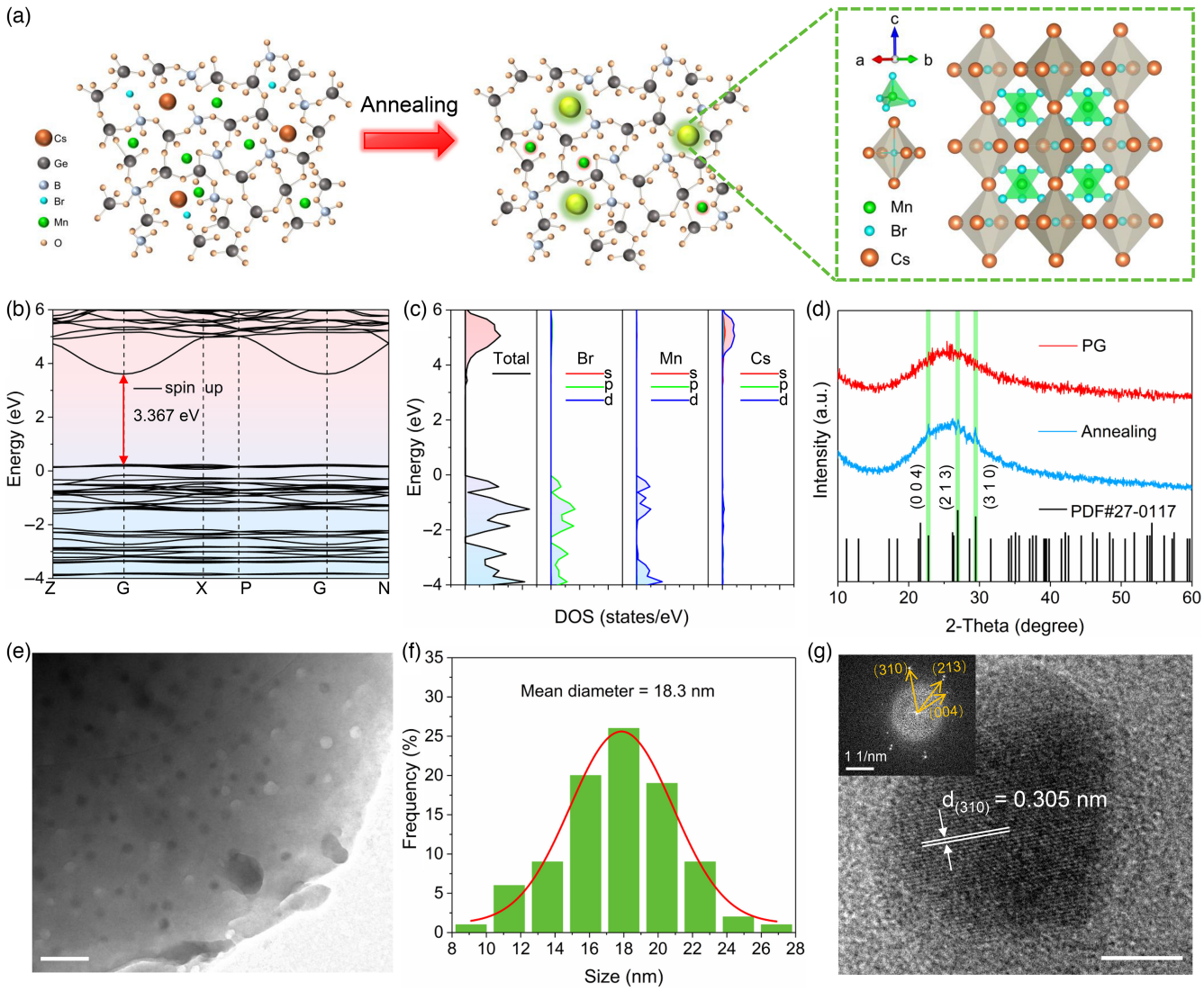

Fig. 1 Structural properties of Cs_3MnBr_5 NCs crystallized in the glass. (a) Schematic diagram of glass network structure before (left) and after (middle) annealing and the anti-perovskite structure of the Cs_3MnBr_5 crystal (right). (b) DFT-calculated band structures and (c) electronic density of states of the Cs_3MnBr_5 crystal. (d) XRD patterns of the PG and the glass sample after annealing at 570°C for 5 h. (e) TEM image, (f) corresponding size distribution, and (g) HRTEM image of the glass annealed at 530°C for 5 h. The inset in (g) is the fast Fourier transform pattern corresponding to the (310), (213), and (004) crystal facet. The scale bars in (e) and (g) are 100 and 10 nm, respectively.

emerges after crystallization, which originates from Mn^{2+} in the tetrahedron of Cs_3MnBr_5 NCs [Fig. 2(c)]. It is worth noting that there are two luminescence centers in the glass after annealing, attributed to Cs_3MnBr_5 NCs and the remaining Mn^{2+} ions in the glass matrix. Thus, the luminescence color can also be adjusted by controlling the excitation wavelength due to the two different luminescence centers, as shown in Fig. 2(d) and Figs. S4(a, b) in the Supplemental Material. The variation of two different emission bands in the time-resolved emission spectrum (1 to 10 ms) shows two different coordination environments around Mn^{2+} in the annealed glass sample (Fig. S5 in the Supplemental Material). With the increase of annealing temperature, the fluorescence lifetimes of the green and red emission change a little [Figs. 2(e) and 2(f)]. This is because Mn^{2+} is in a stable tetragonal and hexagonal field environment, respectively. Due to the crystal coordination environment of Cs_3MnBr_5 NCs, the green emission lifetime reaches the microsecond range, which is often required for dynamical X-ray imaging.

To further increase the concentration of Cs_3MnBr_5 NCs, we also investigated the effect of annealing duration on the luminescence properties of the samples. The glass samples were treated at 570°C for 5 to 40 h, respectively, and a series of photoluminescence (PL) spectra and lifetime decay curves were recorded [Figs. S6(a–d) in the Supplemental Material]. It can be found that with the increase in annealing duration, the green emission of the samples is gradually enhanced due to the increase in the concentration of Cs_3MnBr_5 NCs. However, the scattering caused by the increase in crystal size also leads to

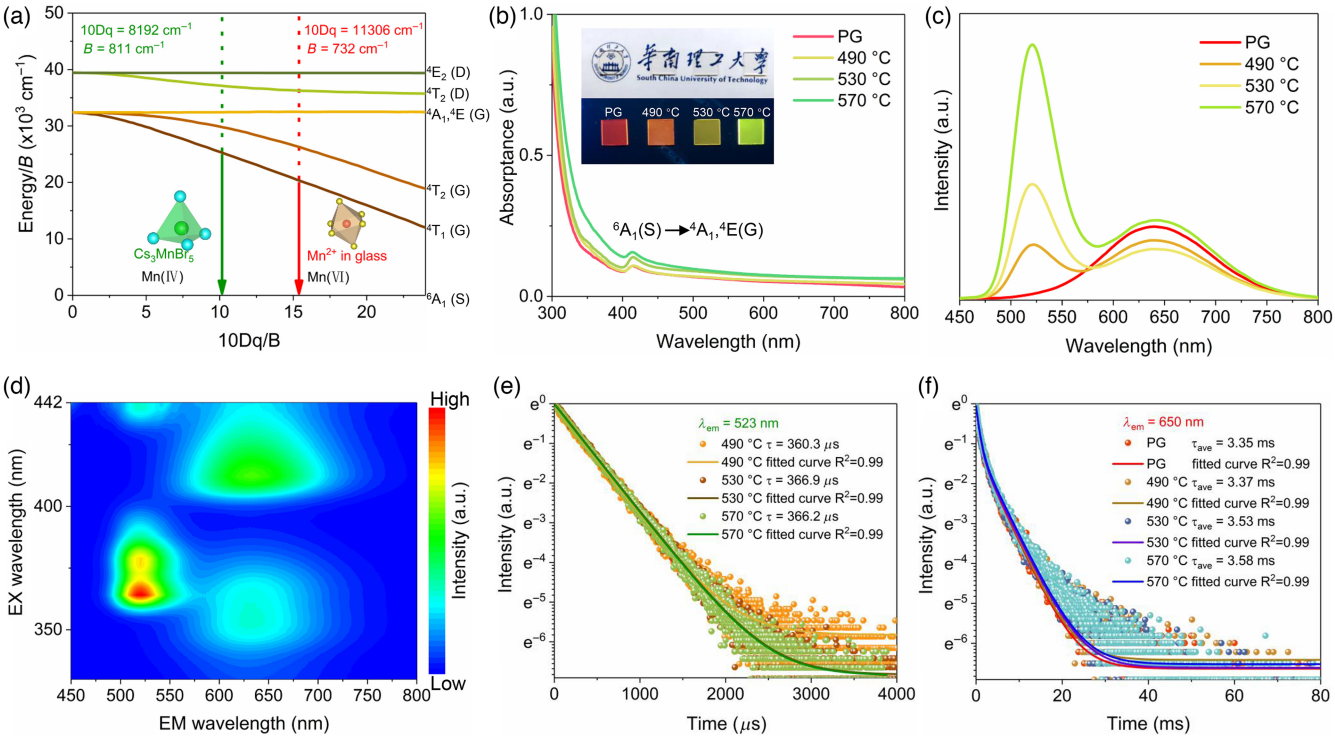

Fig. 2 PL properties of Cs_3MnBr_5 NCs in the glass. (a) Tanabe–Sugano diagram of $3d_5$ electronic configuration of Mn^{2+} ions. (b) Absorption and (c) PL spectra of the PG and samples annealed at different temperatures for 5 h. The inset in (b) shows the photographs of the glass samples taken under daylight (top) and 365 nm UV light (bottom). (d) PLE mapping spectra of the glass sample annealed at 570°C for 5 h. (e) Fluorescence decay curves of Cs_3MnBr_5 NCs and (f) Mn^{2+} in glass annealed at different temperatures. The fitting curves are fitted with (e) single-exponential and (f) double-exponential, respectively. The excitation wavelength used in (c), (e), (f) is 365 nm.

a large optical loss of the glass samples. Thus, the sample treated at 570°C for 10 h has the highest PL quantum yield of 35.5% (Fig. S7 in the Supplemental Material). Depending on the annealing temperature and duration, the emission color of the glass samples can be precisely adjusted from red to green (Fig. S8 in the Supplemental Material). In contrast to the typical $CsPbX_3$ (X = Cl, Br, I) materials, which have poor thermal and optical stability, the stability of Cs_3MnBr_5 NC-embedded glass has been greatly improved. At 503 K, the green emission of the sample retains 66% of the intensity recorded at room temperature [Fig. S9(a, b) in the Supplemental Material]. In addition, under the continuous irradiation of a 375 nm laser with 6.4 W/cm^2 for 60 min, the PL intensity of Cs_3MnBr_5 remained unchanged (Fig. S10(a, b) in the Supplemental Material). These characteristics can be attributed to the unique restriction of the high-density luminescent center in the Cs_3MnBr_5 anti-perovskite configuration and their larger binding energies.

2.3 Radioluminescence Properties of Cs_3MnBr_5 NCs in the Glass

The tunable PL, excellent stability, and large Stokes shift (negligible self-absorption) demonstrate the large potential of Cs_3MnBr_5 NC-embedded glass for applications in the field of X-ray detection applications. In contrast to the PL mechanism, the radioluminescence (RL) mechanism involves an additional photoelectron conversion process that converts high-energy electrons to low-energy ones for radiative recombination [Fig. 3(a)].[15] The X-ray is absorbed by heavy atoms, such as Cs, Mn, Ge from Cs_3MnBr_5 NC-embedded glass through photoelectric effect and Compton scattering. Then, a large number of hot electrons are released and captured by the luminescence center after being thermalized. We investigate the X-ray absorption coefficient of the Cs_3MnBr_5 NC-embedded glass from 1 to 1000 keV. The absorption coefficient of Cs_3MnBr_5 NC-embedded glass is comparable with the typical scintillators, such as $Bi_4Ge_3O_{12}$ (BGO) and $CsPbBr_3$ [Fig. 3(b)].[41] The light yield of Cs_3MnBr_5 NC-embedded glass is ~5200 photons MeV^{-1} estimated by using commercial scintillator BGO as a standard sample (Fig. S11 in the Supplemental Material).[42] Due to the dual-emission centers, the glass samples demonstrate RL with an adjustable red–green ratio under X-ray excitation by adjusting the annealing temperature and duration [Fig. 3(c) and Fig. S12 in the Supplemental Material]. It is shown in Fig. 3(c) that with the increase of annealing duration, the emission color of glass samples changes from light yellow to yellow-green under X-ray irradiation. The Cs_3MnBr_5 NC-embedded glass shows the similar PL and RL spectra, indicating that they originate from the same radiative recombination channel upon X-ray and UV excitation. Interestingly, from the RL spectra recorded under X-ray excitation with different dose rates, we observe that Cs_3MnBr_5 NCs have a better linear response to the dose rate of X-rays than that of Mn^{2+} ions in the glass sample (Fig. S13 in the Supplemental Material). In Fig. 3(d), we show the RL spectra

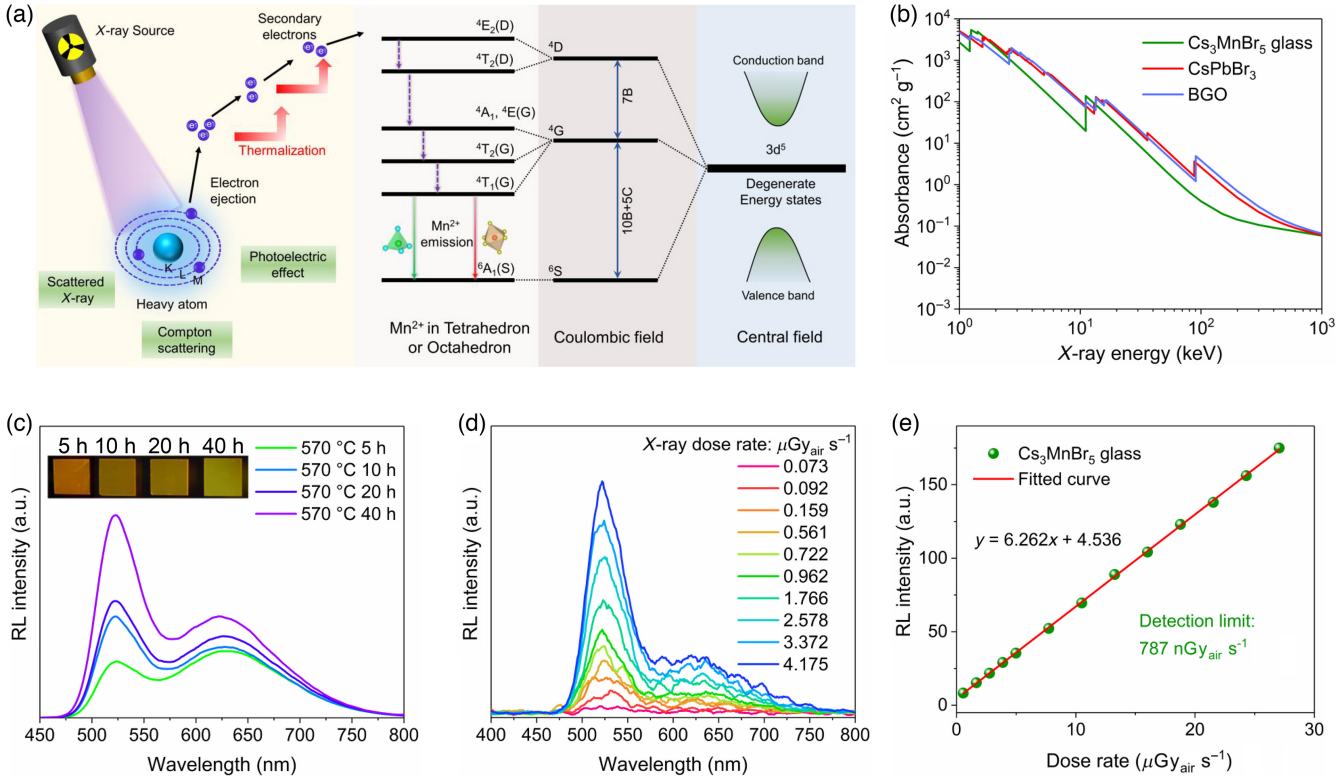

Fig. 3 RL properties of Cs_3MnBr_5 NCs in the glass. (a) Schematic diagram of X-ray-induced luminescence mechanism of Cs_3MnBr_5 NCs and Mn^{2+} ions in the glass. (b) X-ray attenuation efficiency of Cs_3MnBr_5 NC-embedded glass, BGO, and $CsPbBr_3$ crystal. (c) RL spectra of Cs_3MnBr_5 NC-embedded glass annealed at 570°C for different durations recorded under X-ray excitation with a dose rate of 4.814 $mGy_{air}\,s^{-1}$. The inset shows the photographs of the corresponding samples taken under X-ray irradiation. (d) RL spectra of the sample annealed at 570°C for 40 h recorded under different low X-ray dose rates. (e) Linear relationship between the low dose rate and RL intensity of the sample annealed at 570°C for 40 h.

of a series of low-dose X-ray excitations. For scintillation materials, the detection limit is one of the most important parameters for medical examination. Here, the detection limit of the X-ray dose rate is 787 $nGy_{air}\,s^{-1}$ for Cs_3MnBr_5 NC-embedded glass when the signal-to-noise ratio is 3. This value is significantly lower than the dose rate used in X-ray medical diagnosis (5.5 $\mu Gy_{air}\,s^{-1}$ dose rate), as shown in Fig. 3(e).[43] Therefore, these merits of Cs_3MnBr_5 NC-embedded glass make it possible to achieve high-performance X-ray detection and real-time X-ray imaging.

2.4 X-Ray Imaging Performance of Cs_3MnBr_5 NCs in the Glass

Due to the high optical transparency of glass (Fig. S14 in the Supplemental Material) and the excellent RL properties, this Cs_3MnBr_5 NC-embedded glass is used for high-resolution X-ray imaging. Here, we construct a self-made X-ray imaging system [Fig. 4(a)], and a series of objects, such as an AI chip, a charging cable, and a circuit board, were imaged by Cs_3MnBr_5 NC-embedded glass under X-ray and captured by a commercial digital camera. As shown in Fig. 4(b), the internal structures are directly observed, indicating that Cs_3MnBr_5 NC-embedded glass is promising for electronics inspection and damage imaging. To further demonstrate the X-ray imaging capability of Cs_3MnBr_5 NC-embedded glass, images of the standard X-ray resolution pattern plate with different thicknesses of glasses were used (Fig. S15 in the Supplemental Material). The highest resolution of the X-ray image was achieved while the glass thickness is 0.6 mm (Fig. S16 in the Supplemental Material). The observation down-limit is between 18 and 20 $lp\,mm^{-1}$, which is consistent with the calculated results of modulation transfer functions (MTFs) according to the slanted-edge method [Fig. 4(d) and Fig. S17 in the Supplemental Material]. Due to the high transparency of the glass, the high X-ray luminescence efficiency and the negligible self-absorption effect of Cs_3MnBr_5 NCs, the spatial resolution of our glass sample reaches 19.1 $lp\,mm^{-1}$ at MTF = 0.2, which exceeds most recently reported materials for X-ray imaging [Fig. 4(e)]. In addition, real-time radiography was successfully performed by recording the rotation procedure of an iron spring with an angular velocity of $\pi/12$ $rad\,s^{-1}$. As shown in Fig. 4(f) and Video 1, we can see the image of the rotary spring, further confirming the high-quality and rapid X-ray imaging based on the Cs_3MnBr_5 NC-embedded glass.

2.5 Ultrastable X-Ray Imaging Application

Owing to the encapsulation by the glass medium and the stability of the anti-perovskite structures, the Cs_3MnBr_5 NC-

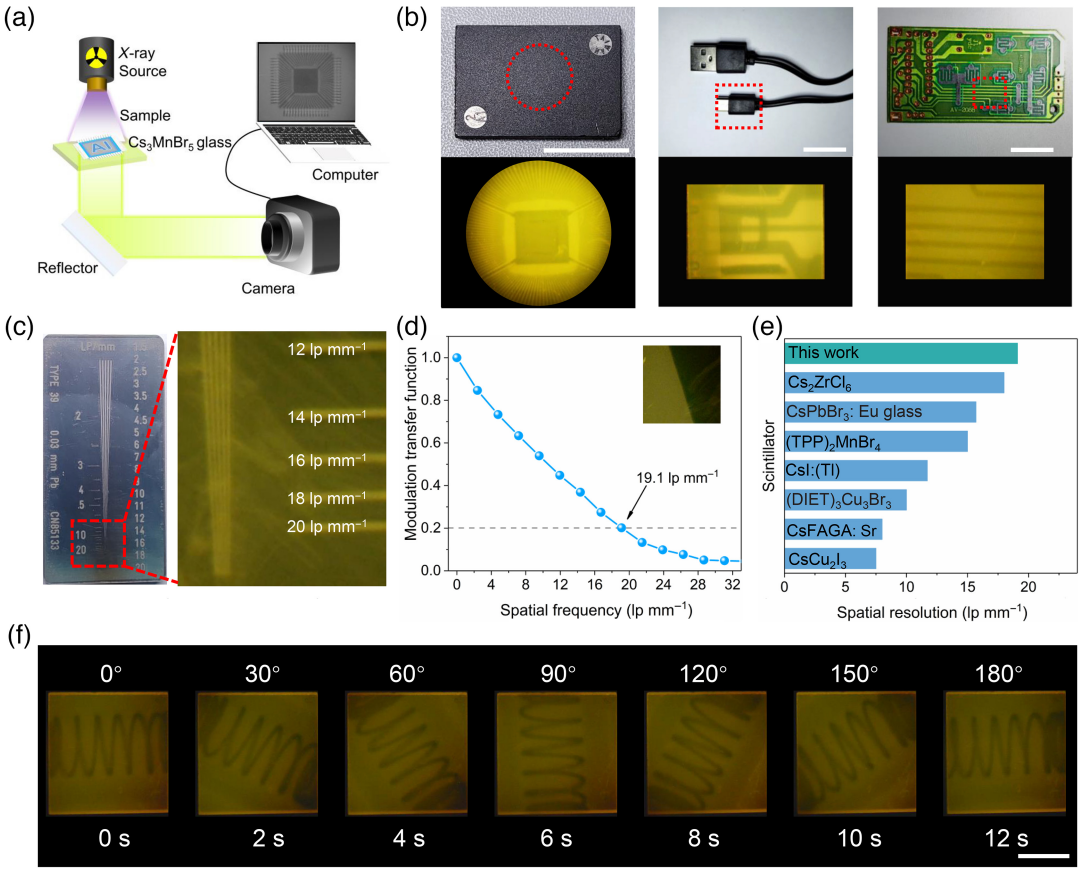

Fig. 4 Demonstrations for real-time radiography. (a) The schematic of the X-ray imaging system. (b) Photographs of an Al chip (left), charging cable (middle), and circuit board (right) under daylight and X-ray irradiation. Scale bars, 1 cm. (c) Bright-field and X-ray images of the standard X-ray resolution pattern plate with the Cs_3MnBr_5 NC-embedded glass. (d) MTF of X-ray images obtained from the Cs_3MnBr_5 NC-embedded glass (the thickness is 0.6 mm). (e) Comparisons of spatial resolutions in representative scintillators.[9,16–18,44–46] (f) Real-time dynamic X-ray images recording the procedure of two-dimensional rotation of an iron spring; the speed of angular velocity is $\pi/12$ rad s^{-1} (Video 1, MP4, 14 MB [URL: https://doi.org/10.1117/1.AP.5.4.046002.s1]). Scale bar, 5 mm.

embedded glass is expected to be used for X-ray imaging applications in medical fields and space stations. Moreover, we are surprised to find that the Cs_3MnBr_5 NC-embedded glass has very stable X-ray-excited optical properties when tested in a variety of harsh environments. The temperature-dependent RL spectra of Cs_3MnBr_5 NC-embedded glass are shown in Figs. 5(a) and 5(b). It can be found that at temperature up to 563 K, the RL intensity of red emission from Mn^{2+} in the glass drops sharply, while the green emission from Cs_3MnBr_5 NCs retains 73% of the room temperature intensity. In addition, the high thermal stability is further supported by the periodic change in emission intensity under repeated heating/cooling from 303 to 563 K for six cycles, as shown in Fig. 5(c). The excellent RL stability of Cs_3MnBr_5 NC-embedded glass in high-temperature environment exceeds most recently reported materials for X-ray imaging (Table S1 in the Supplemental Material). These results indicate that Cs_3MnBr_5 NC-embedded glass possesses strong thermal stability.

We continue with a series of demonstrations of the imaging performance of the Cs_3MnBr_5 NC-embedded glass in different environments. First, an iron spring is encapsulated in an ABS cylindrical resin and placed together with the Cs_3MnBr_5 NC-embedded glass in a 1 cm × 1 cm × 10 cm colorimetric dish filled with dimethyl silicone oil [Fig. 5(d)]. The spring inside is not visible under daylight but can be imaged by Cs_3MnBr_5 NC-embedded glass under X-ray irradiation. In addition, the X-ray images of the spring can be detected at different temperatures, benefited by the stable thermal RL property of Cs_3MnBr_5 NC-embedded glass [Fig. 5(e)]. In this experiment, the temperature of the Cs_3MnBr_5 NC-embedded glass is detected by using an infrared camera. The X-ray image at the temperature up to 121.6°C is still clear, indicating that the Cs_3MnBr_5 NC-embedded glass can be used for high-temperature X-ray imaging. In another experiment, we place an integrated circuit chip and the Cs_3MnBr_5 NC-embedded glass in deionized water and recorded the underwater X-ray imaging for 24 h [Fig. S18(a, b) in the Supplemental Material]. After the Cs_3MnBr_5 NC-embedded glass was immersed in deionized water for 0, 5, 15, and 24 h, the X-ray images of the internal structure of the chip are still clear. Moreover, the underwater X-ray images remain unchanged at different temperatures (Fig. S19 in the Supplemental Material). Figure 5(f) presents

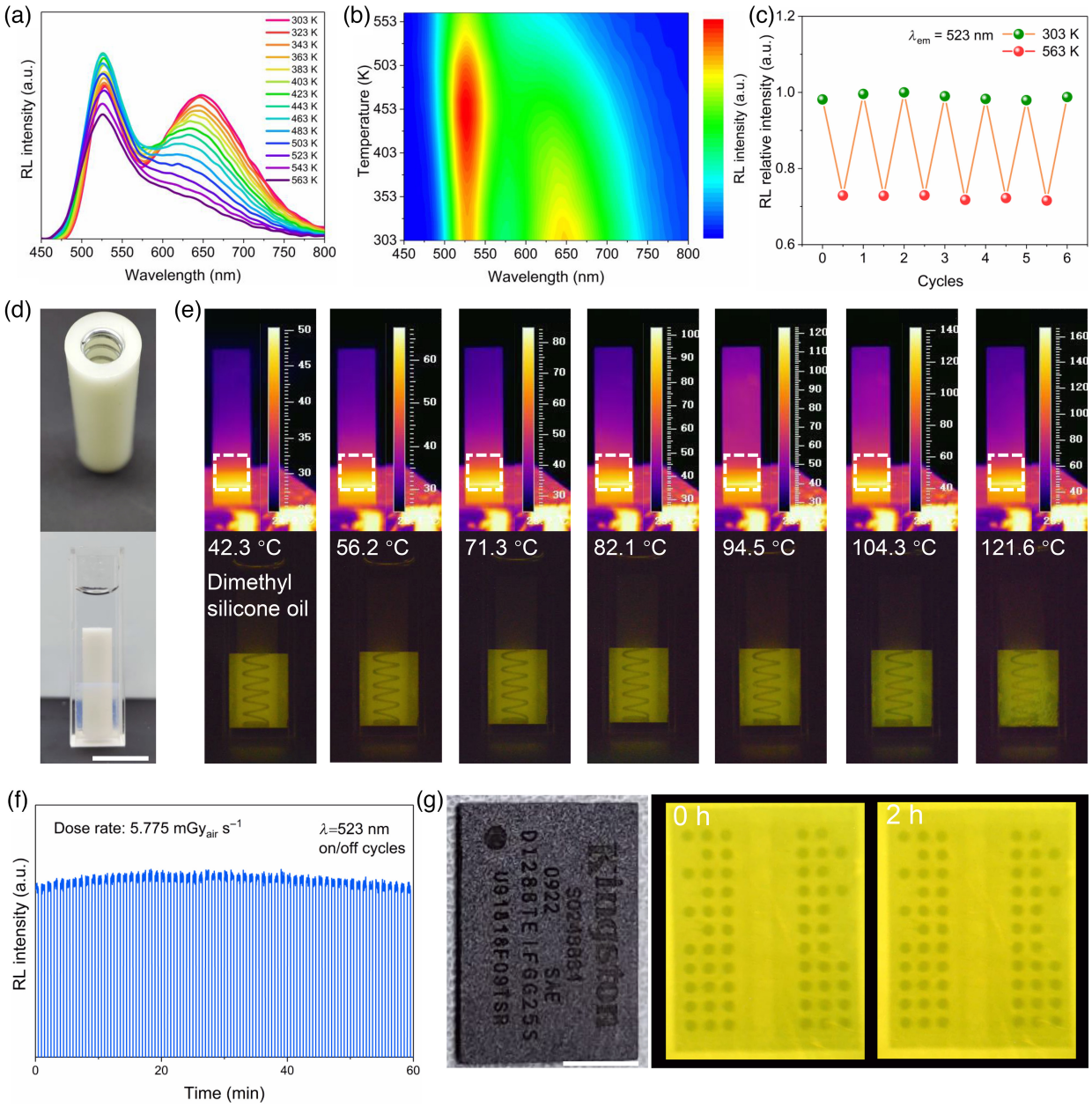

Fig. 5 Ultrastable X-ray imaging. (a) Temperature-dependent RL spectra and (b) emission mapping of the glass sample under X-ray irradiation with a dose rate of 4.814 $mGy_{air}\ s^{-1}$. (c) RL intensity of the Cs_3MnBr_5 NCs in the glass sample upon six heating/cooling cycling processes over the temperature ranging from 303 to 563 K. (d) Photographs of a cylindrical ABS resin embedded with an iron spring in the air (top) and dimethyl silicone oil (bottom). (e) Thermal imaging photographs (top) and X-ray images (bottom) of the cylindrical ABS resin embedded with an iron spring immersed in dimethyl silicone oil at different temperatures. Scale bar, 1 cm. (f) RL intensity of Cs_3MnBr_5 NCs in the glass recorded over continuous 120 on/off cycles during 60 min. (g) Photograph (left) and X-ray images (right) of the chip taken under continuous irradiation for 2 h. Scale bar, 2 mm.

the RL intensity of Cs_3MnBr_5 NC-embedded glass recorded under repeated high-dose X-ray (5.775 $mGy_{air}\ s^{-1}$) excitation. It can be seen that after 120 on–off cycles, the RL intensity remains unchanged, showing good long-term X-ray irradiation stability. Moreover, even under a higher dose rate up to 9.66 $mG_{air}\ s^{-1}$, its luminescence was only slightly affected for a short time (Fig. S20 in the Supplemental Material). In addition, the X-ray images from Cs_3MnBr_5 NC-embedded glass can still be observed after continuous X-ray irradiation for 2 h at a high dose rate up to 5.775 $mGy_{air}\ s^{-1}$ [Fig. 5(g)]. Considering the above X-ray imaging demonstrations in different environments, the Cs_3MnBr_5 NC-embedded glass is

expected to be applied for the next generation of scintillation materials.

3 Conclusion

In summary, we have successfully prepared an ultrastable monolithic scintillator based on a lead-free Cs_3MnBr_5 anti-perovskite NC-embedded glass. The experimental results show that the Cs_3MnBr_5 NC-embedded glass has high optical transmittance, excellent tunable optical properties, and durable stability. Therefore, the Cs_3MnBr_5 NC-embedded glass can achieve an X-ray detection limit of 767 $nGy_{air}\,s^{-1}$, high X-ray imaging spatial resolution of 19.1 $lp\,mm^{-1}$, and excellent stability under high-dose X-ray irradiation. The Cs_3MnBr_5 NC-embedded glass can be made into optical fibers, so the X-ray imaging performance and resolution may be further improved by using the pixelated dual tapered fiber arrays method.[47] More importantly, with the protection of the glass matrix and the stability of the anti-perovskite structure, we demonstrate high-resolution X-ray imaging under a high-temperature and humidity environment by using Cs_3MnBr_5 NC-embedded glass. Our findings not only provide an effective strategy for achieving ultrastable X-ray-excited luminescence in a harsh environment but also broaden the applications of lead-free anti-perovskite materials in the applications of advanced X-ray radiography.

4 Appendix A: Sample Preparation

The glass samples were fabricated by using the melting-quenching method. Reagent-grade raw materials including GeO_2, B_2O_3, ZnO, $CaCO_3$, NaBr, Cs_2CO_3, and MnO (glass composition: $37GeO_2$-$31B_2O_3$-3CaO-2ZnO-3MnO-$6Cs_2O$-18NaBr) were mixed and then melted at 1100°C. The PG was made by pouring the melt into a mold. Then the glass was annealed at 350°C for 5 h and cooled for 10 h to room temperature to release the thermal stress. The PG samples were cut after removal from the mold and well-polished for crystallization of Cs_3MnBr_5 anti-perovskite NCs by annealing at 490°C, 530°C, and 570°C.

5 Appendix B: Sample Characterization

Differential scanning calorimetry was measured by an STA449C Jupiter (Netzsch, Bavaria, Germany) in an air atmosphere with a heating rate of 10°C min^{-1}. The XRD patterns were recorded by a D8 ADVANCE X-ray diffractometer (Bruker, Faellanden, Switzerland) with Cu/K_α ($\lambda = 0.1541$ nm) radiation. Absorption spectra were measured on a Lambda 900 (Perkin Elmer, Waltham, MA) spectrophotometer. An Edinburgh FLS 920 instrument (Edinburgh Instruments Ltd., Livingston, United Kingdom) equipped with a photomultiplier tube for light detection (Hamamatsu, Japan) was used to measure the PL spectra, excitation spectra, and lifetime decay of bulk glass sample. A 450 W ozone-free xenon lamp and a microsecond-pulsed xenon flash lamp were used as excitation sources during PL and lifetime decay measurement, respectively. For thermal and optical stability tests, PL spectra were excited by a 375 nm laser and recorded by an Ocean Optics HR4000 spectrometer. XPS measurements were performed on an Axis Ultra DLD XPS instrument (Kratos, England) with a monochromatic Al K_α source (1486.6 eV). The morphology and size distribution of Cs_3MnBr_5 NCs were measured by transmission electron microscopy (TEM, JEM-2100F, JEOL, Japan). The glass sample after crystallization was put into an agate mortar and ground to powder in ethanol for 20 min, and then dispersed in ethanol with ultrasonic treatment for 10 min. Finally, three to five drops of supernatant were dropped on the copper net for the TEM image test. The model of the electric rotary displacement table used for real-time imaging was Thorlabs PRM1Z8. FLS1000 spectrofluorometer (Edinburgh Instruments Ltd., United Kingdom) equipped with an X-ray tube (MAGPRO, Moxtek, W target and tube voltage 50 kV) is used to measure the RL spectra. The digital camera used for X-ray imaging is a Nikon d610.

6 Appendix C: Calculation of the X-Ray Attenuation Coefficients

The detail of calculation is fully described in the subsection entitled "Supplementary Note 2" in the Supplemental Material.

Code, Data, and Material Availability

Data underlying the results presented in this paper may be obtained from the corresponding author upon reasonable request. All software is also available from the corresponding author upon reasonable request.

Acknowledgments

This work was financially supported by the National Natural Science Foundation of China (62122027, 52002128, 62075063, 62205109, 12204179, 52202004), Key R&D Program of Guangzhou (202007020003), fellowship of the China Postdoctoral Science Foundation (2022M711185, 2021M691054), National Postdoctoral Program for Innovative Talents of China (BX20220113), Guangdong Basic and Applied Basic Research Foundation (2021A1515110911, 2021A1515110475, 2022A1515011289, 2023A1515012666), Local Innovative and Research Teams Project of Guangdong Pearl River Talents Program (2017BT01X137), Fundamental Research Funds for the Central Universities (2022ZYGXZR030), Guangzhou Basic and Applied Basic Research Foundation (202201010428), and State Key Laboratory of Luminescent Materials and Devices, South China University of Technology. The authors declare no competing interests.

References

1. J. A. Rowlands, "Material change for X-ray detectors," *Nature* **550**(7674), 47–48 (2017).
2. J. Pang et al., "Vertical matrix perovskite X-ray detector for effective multi-energy discrimination," *Light Sci. Appl.* **11**(1), 105 (2022).
3. J. Jiang et al., "Synergistic strain engineering of perovskite single crystals for highly stable and sensitive X-ray detectors with low-bias imaging and monitoring," *Nat. Photonics* **16**(8), 575–581 (2022).
4. J. Perego et al., "Composite fast scintillators based on high-*Z* fluorescent metal–organic framework nanocrystals," *Nat. Photonics* **15**(5), 393–400 (2021).
5. S. Cho et al., "Hybridisation of perovskite nanocrystals with organic molecules for highly efficient liquid scintillators," *Light Sci. Appl.* **9**(1), 156 (2020).
6. Q. Chen et al., "All-inorganic perovskite nanocrystal scintillators," *Nature* **561**(7721), 88–93 (2018).
7. X. Huang et al., "Reversible 3D laser printing of perovskite quantum dots inside a transparent medium," *Nat. Photonics* **14**(2), 82–88 (2020).

8. H. Zhang et al., "Reproducible X-ray imaging with a perovskite nanocrystal scintillator embedded in a transparent amorphous network structure," *Adv. Mater.* **33**(40), 2102529 (2021).
9. W. Ma et al., "Highly resolved and robust dynamic X-ray imaging using perovskite glass-ceramic scintillator with reduced light scattering," *Adv. Sci.* **8**(15), 2003728 (2021).
10. J. Yuan et al., "How to apply metal halide perovskites to photocatalysis: challenges and development," *Nanoscale* **13**(23), 10281–10304 (2021).
11. M. Li and Z. Xia, "Recent progress of zero-dimensional luminescent metal halides," *Chem. Soc. Rev.* **50**(4), 2626–2662 (2021).
12. S. Cheng et al., "Ultrabright and highly efficient all-inorganic zero-dimensional perovskite scintillators," *Adv. Opt. Mater.* **9**(13), 2100460 (2021).
13. M. Hunyadi et al., "Scintillator of polycrystalline perovskites for high-sensitivity detection of charged-particle radiations," *Adv. Funct. Mater.* **32**(48), 2206645 (2022).
14. B. Yang et al., "Lead-free halide Rb_2CuBr_3 as sensitive X-ray scintillator," *Adv. Mater.* **31**(44), 1904711 (2019).
15. W. Zhu et al., "Low-dose real-time X-ray imaging with nontoxic double perovskite scintillators," *Light Sci. Appl.* **9**(1), 112 (2020).
16. F. Zhang et al., "Thermally activated delayed fluorescence zirconium-based perovskites for large-area and ultraflexible X-ray scintillator screens," *Adv. Mater.* **34**(43), 2204801 (2022).
17. K. Han et al., "Seed-crystal-induced cold sintering toward metal halide transparent ceramic scintillators," *Adv. Mater.* **34**(17), 2110420 (2022).
18. B. Li et al., "Zero-dimensional luminescent metal halide hybrids enabling bulk transparent medium as large-area X-ray scintillators," *Adv. Opt. Mater.* **10**(10), 2102793 (2022).
19. Q. Kong et al., "Phase engineering of cesium manganese bromides nanocrystals with color-tunable emission," *Angew. Chem. Int. Ed. Engl.* **60**(36), 19653–19659 (2021).
20. K. Li et al., "Ultra-stable and color-tunable manganese ions doped lead-free cesium zinc halides nanocrystals in glasses for light-emitting applications," *Nano Res.* **15**(10), 9368–9376 (2022).
21. Y. Wang et al., "Antiperovskites with exceptional functionalities," *Adv. Mater.* **32**(7), 1905007 (2020).
22. D. Han et al., "Design of high-performance lead-free quaternary antiperovskites for photovoltaics via ion type inversion and anion ordering," *J. Am. Chem. Soc.* **143**(31), 12369–12379 (2021).
23. H. K. Singh et al., "High-throughput screening of magnetic antiperovskites," *Chem. Mater.* **30**(20), 6983–6991 (2018).
24. J. Zheng et al., "Antiperovskite K_3OI for K-ion solid state electrolyte," *J. Phys. Chem. Lett.* **12**(30), 7120–7126 (2021).
25. N. Hoffmann et al., "Superconductivity in antiperovskites," *NPJ Comput. Mater.* **8**(1), 150 (2022).
26. S. Tan et al., "An antiperovskite compound with multifunctional properties: Mn_3PdN," *Int. J. Heat. Mass. Transf.* **302**, 122389 (2021).
27. S. Yan et al., "Light-emitting diodes with manganese halide tetrahedron embedded in anti-perovskites," *ACS Energy Lett.* **6**(5), 1901–1911 (2021).
28. M. Kogia et al., "High temperature shear horizontal electromagnetic acoustic transducer for guided wave inspection," *Sensors* **16**(4), 582 (2016).
29. T. Fukuchi et al., "Nondestructive inspection of thermal barrier coating of gas turbine high temperature components," *IEEJ Trans. Electr. Electron. Eng.* **11**(4), 391–400 (2016).
30. R. Kuhn et al., "Measuring device for synchrotron X-ray imaging and first results of high temperature polymer electrolyte membrane fuel cells," *J. Power Sources* **196**(12), 5231–5239 (2011).
31. F. Akitomo et al., "Investigation of effects of high temperature and pressure on a polymer electrolyte fuel cell with polarization analysis and X-ray imaging of liquid water," *J. Power Sources* **431**, 205–209 (2019).
32. Y. Wang et al., "*In situ* high-pressure and high-temperature X-ray microtomographic imaging during large deformation: a new technique for studying mechanical behavior of multiphase composites," *Geosphere* **7**(1), 40–53 (2011).
33. M. Yao et al., "High-temperature stable $FAPbBr_3$ single crystals for sensitive X-ray and visible light detection toward space," *Nano Lett.* **21**(9), 3947–3955 (2021).
34. V. S. Devahdhanush et al., "Experimental heat transfer results and flow visualization of vertical upflow boiling in Earth gravity with subcooled inlet conditions: in preparation for experiments onboard the international space station," *Int. J. Heat. Mass. Transf.* **188**, 122603 (2022).
35. L. Shao et al., "Broadband ultraviolet photodetectors based on cerium doped lead-free Cs_3MnBr_5 metal halide nanocrystals," *ACS Sustain. Chem. Eng.* **9**(14), 4980–4987 (2021).
36. Y. Wu et al., "New photoluminescence hybrid perovskites with ultrahigh photoluminescence quantum yield and ultrahigh thermostability temperature up to 600 K," *Nano Energy* **77**, 105170 (2020).
37. R. Baran, L. Valentin, and S. Dzwigaj, "Incorporation of Mn into the vacant T-atom sites of a BEA zeolite as isolated, mononuclear Mn: FTIR, XPS, EPR and DR UV-Vis studies," *Phys. Chem. Chem. Phys.* **18**(17), 12050–12057 (2016).
38. L. Q. Guan et al., "All-inorganic manganese-based $CsMnCl_3$ nanocrystals for X-ray imaging," *Adv. Sci.* **9**(18), 2201354 (2022).
39. S. Lv et al., "Transition metal doped smart glass with pressure and temperature sensitive luminescence," *Adv. Opt. Mater.* **6**(21), 1800881 (2018).
40. S. Lin et al., "High-security-level multi-dimensional optical storage medium: nanostructured glass embedded with $LiGa_5O_8$: Mn^{2+} with photostimulated luminescence," *Light Sci. Appl.* **9**(1), 22 (2020).
41. T. Jiang et al., "Highly efficient and tunable emission of lead-free manganese halides toward white light-emitting diode and X-ray scintillation applications," *Adv. Funct. Mater.* **31**(14), 2009973 (2021).
42. T. Ji et al., "Ce^{3+}-doped yttrium aluminum garnet transparent ceramics for high-resolution X-ray imaging," *Adv. Opt. Mater.* **10**(6), 2102056 (2022).
43. H. Wei et al., "Sensitive X-ray detectors made of methylammonium lead tribromide perovskite single crystals," *Nat. Photonics* **10**(5), 333–339 (2016).
44. W. F. Wang et al., "Sensitive X-ray detection and imaging by a scintillating lead(II)-based metal-organic framework," *Chem. Eng. J.* **430**, 133010 (2022).
45. M. Zhang et al., "Oriented-structured $CsCu_2I_3$ film by close-space sublimation and nanoscale seed screening for high-resolution X-ray imaging," *Nano Lett.* **21**(3), 1392–1399 (2021).
46. X. Ou et al., "High-resolution X-ray luminescence extension imaging," *Nature* **590**(7846), 410–415 (2021).
47. L. Yi et al., "A double-tapered fibre array for pixel-dense gamma-ray imaging," *Nat. Photonics* **17**, 494–500 (2023).
48. A. K. Mehra, "Trees correction matrices for d5 configuration in cubic symmetry," *J. Chem. Phys.* **48**(10), 4384–4386 (1968).
49. J. L. Rao and K. Purandar, "Electronic absorption spectrum of Mn^{2+} ions doped in diglycine barium chloride monohydrate," *Solid State Commun.* **37**(12), 983 (1981).
50. F. Cao et al., "Shining emitter in a stable host: design of halide perovskite scintillators for X-ray imaging from commercial concept," *ACS Nano* **14**(5), 5183–5193 (2020).
51. J. Jin et al., "Zn^{2+} doping in organic manganese(II) bromide hybrid scintillators toward enhanced light yield for X-ray imaging," *Adv. Opt. Mater.*, 2300330 (2023).
52. T. C. Wang et al., "High thermal stability of copper-based perovskite scintillators for high-temperature X-ray detection," *ACS Appl. Mater. Interfaces* **15**(19), 23421–23428 (2023).
53. X. Li et al., "Mn^{2+} induced significant improvement and robust stability of radioluminescence in $Cs_3Cu_2I_5$ for high-performance nuclear battery," *Nat. Commun.* **12**(1), 3879 (2021).

Yakun Le is pursuing his PhD under the supervision of Prof. Guoping Dong, at the School of Materials Science and Engineering from the South China University of Technology (SCUT). His research focuses on metal halide nanocrystal-in-glass composite and their advanced optical applications.

Guoping Dong received his MS (2007) and PhD (2010) from Wuhan University of Technology and Shanghai Institute of Optics and Fine Mechanics (CAS), respectively. Then he worked in South China University of Technology (SCUT) as a research assistant (2010) and associate professor (2011). He is currently a full professor (2014) in State Key Laboratory of Luminescent Materials and Devices at SCUT. His research focuses on design, preparation, and optoelectronic properties of optical functional materials and devices.

Biographies of the other authors are not available.